Characterization of plasmas produced by a laser line focus

M. D. J. Burgess, R. Dragila, B. Luther-Davies, K. A. Nugent, A. J. Perry, and G. J. Tallents
Department of Engineering Physics, Research School of Physical Sciences, The Australian National University, Canberra, Australian Capital Territory 2601, Australia

M. C. Richardson and R. S. Craxton
Laboratory for Laser Energetics, The University of Rochester, 250 East River Road, Rochester, New York 14623
(Received 24 June 1985)

Plasmas produced from cylindrical and planar targets by line-focused 30-ps-duration, high-intensity ($\sim 10^{14}$ W/cm^2), 1064-nm laser pulses have been characterized with a number of diagnostics. Detailed measurements of the morphology and expansion of the electron-density profile were made with picosecond interferometry and compared with predictions of a two-dimensional Eulerian hydrodynamic code. Microscopic filamentation structure in the center regions of the corona, and the generation of a density plateau at $n_c/4$, were features consistently observed which lack quantitative explanations. The implications of these observations for the production of optimum plasma conditions suitable for recombination or collisionally excited x-ray laser schemes are discussed.

INTRODUCTION

In studies of x-ray laser schemes utilizing laser-produced plasmas as the gain medium,[1] there are often distinct advantages to creating long linear plasmas with large aspect ratios. Namely, they permit the clear spectroscopic delineation of gain along and across the plasma, they maximize gain along the line axis, and the population densities of the quantum states involved in the lasing are not greatly affected by resonance-line optical opacity (which can destroy the population inversion itself[2]) as the resonance x rays can readily escape across the plasma. Line plasmas can be formed using an astigmatic lens, or a combination of lenses, to focus the laser beam into a line upon the target.[3] The overall shape and character of the line plasma is in most cases of importance to the x-ray laser scheme. In particular, the spatial and temporal distributions of the electron and ion densities and the electron temperature critically determine the local conditions for radiative and collisional excitation and deexcitation, and ultimately population inversion. Recombination laser schemes[4] are particularly sensitive to such issues, as population inversion and x-ray gain conditions are predicted to be possible only under highly transient plasma conditions. Previously published experimental x-ray laser studies which have used line-focused plasmas[2,5] have paid only cursory attention to examination of the plasma conditions and comparison with detailed two-dimensional hydrodynamic code predictions. Recently, laser action was reported on $3p$-$2s$ transitions in Ne-like Se and Y in plasmas created from thin foil targets irradiated with the line-focused 531-nm output of the two-beam Novette facility.[6]

In this paper, we report results of experiments which characterize plasmas created on solid targets by focusing the output of a 1.06-μm, 1.5-J, 75-GW laser onto a line of dimensions 500×20 μm^2. A detailed diagnosis of plasma conditions was made through a number of techniques, including picosecond interferometry of the spatial extent of the electron-density profile, picosecond polarimetry of microscopic magnetic-field structures, box-calorimeter measurements of the overall absorption, x-ray photography of the emitting region of the plasma, x-ray bremsstrahlung measurements of suprathermal electron generation, and the diagnosis of parametric processes through self-generated harmonic-emission analysis. The results have been compared with predictions of the plasma parameters made in cylindrical geometry in one and two dimensions using the Eulerian code SAGE.[7]

EXPERIMENTAL CONDITIONS

These experiments utilized the 85-mm-diam output beam from the 1.06-μm Australian National University (ANU) Nd:glass laser,[8] which provided 1—2 J of energy in pulses with nominal durations of 20 ps and with a pulse-to-background contrast level of $\gtrsim 10^6$. When focused with an $f/1$ spherical lens, this laser has produced peak intensities of $\gtrsim 10^{18}$ W/cm^2 in focal-spot sizes of ≈ 2.1 μm.[8] For the present experiments the laser output was focused into a line using a single-element $f/3$ astigmatic lens. This lens had one surface for spherical focusing, while the other surface had a weak cylindrical curvature to produce line-focus conditions with an aspect ratio of $\sim 100{:}1$. The intensity distribution in the focal plane was measured by reimaging the focus, using an $X5$ flat-field microscope objective with an overall magnification of $X29$, onto a multiple-image camera after attenuation of the input beam. The intensity distribution recorded on Kodak high-speed ir film was digitized using a Perkin-Elmer PDS (Photometric Data Systems) microdensitometer and coverted to an iso-intensity contour plot after correction for the measured film response [Fig. 1(a)]. Single-dimensional transverse lineouts at various positions along the line focus are shown in Fig. 1(b). The beam intensity was found to vary slowly over a region ~ 500 μm

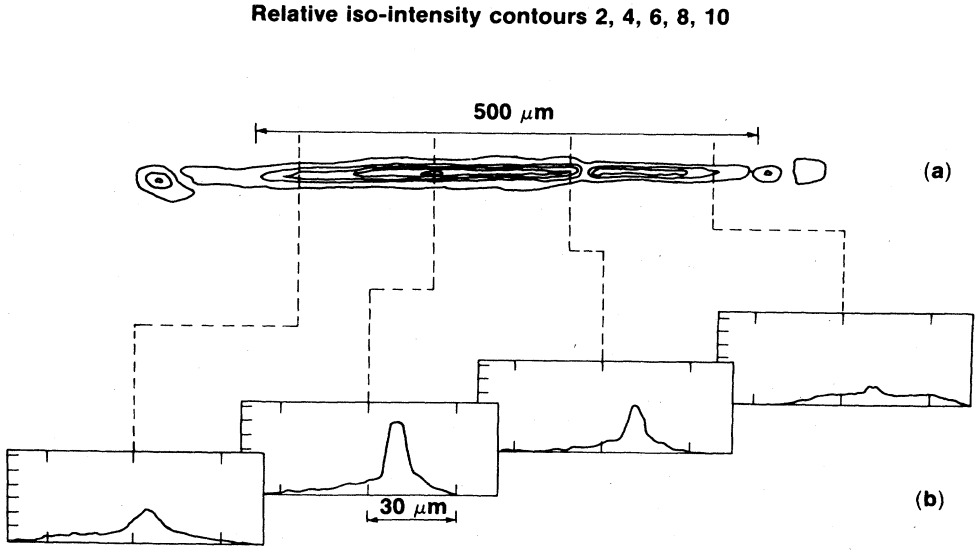

FIG. 1. Details of the measured intensity distribution in the target plane. The iso-intensity contour plot (a) shows the intensity distribution on target at best focus. One-dimensional lineouts at various positions along the distribution are shown in (b).

long by ~ 15 μm wide (half-intensity points) which contained ~ 40—50% of the laser energy. No strong microscopic fine-scale modulation along the length of the intensity distribution was evident. Peak intensities were in the range 5×10^{14}—7×10^{14} W/cm^2. A photograph of x-ray emission in the ~ 1 keV range from a planar solid Al target, obtained with a single-channel Kirkpatrick-Baez reflective microscope, is shown in Fig. 2. A scan through the image close to the center of the field of view showed the half-width of the emitting region was 15—20 μm, in close agreement with the measured focal spot width.

A number of different targets were irradiated. These included (a) Al disks ~ 500 μm in diameter, (b) carbon foils of thickness 1000, 500, or 250 Å, some with 100-Å Au undercoats, supported on thin metallic washers, and (c) solid carbon fibers of ~ 10-μm diameter. Quantitative measurements of the electron-density profile could only be obtained using the carbon fiber targets, where the plasma could be assumed to have the cylindrical symmetry necessary in order to invert the interferometric data. Conversely, the thermal and suprathermal components of the electron energy could only be measured through the bremsstrahlung spectrum for the Al disk targets, since the x-ray emission from the fiber was below the sensitivity of the x-ray detectors at higher photon energies ($h\nu > 2$ keV). Absorption measurements were made with both fiber and disk targets for both s polarization (electric vector along the axis of the line) and p polarization (electric vector normal to the axis of the line). The combination of an enclosing box calorimeter [Fig. 3(a)] with transmitted-light and backscatter-light calorimeters was used to collect the nonabsorbed laser light over $\sim 90\%$ of the full solid angle. The cross-calibration error introduced an uncertainty into the absolute values of absorption of $\sim \pm 3\%$.

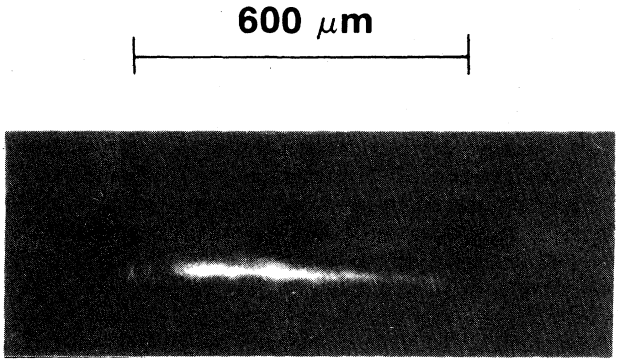

FIG. 2. X-ray micrograph of a line-focused plasma produced from a solid Al target, obtained with a Kirkpatrick-Baez microscope sensitive to x rays in the ~ 1-keV range.

ABSORPTION MEASUREMENTS

Measurements made on disk and fiber targets with s- and p-polarized radiation showed, within the scatter of the experimental data, little dependence of the absorption on polarization. In the case of the carbon fiber targets, whose diameter was much less than the minimum beam width, a large fraction of the incident beam [$\sim 50\%$, see Fig. 3(b)] passed around the target within the cone angle of the incident beam. At best focus the absorbed fraction was $21\pm4\%$, which as a fraction of the energy intercepted by the target is in agreement with data obtained using the glass disks where the absorption was $45\pm5\%$ [Fig. 3(c)], for normal incidence. Figure 3(c) also shows the angular dependence of the absorption on glass disk targets, for the line focus in the plane of the target and for p polarization. This angular dependence is rather weak, but it

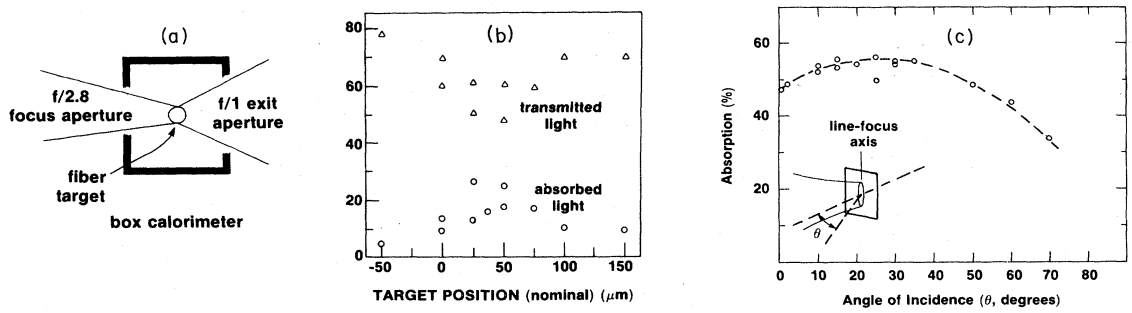

FIG. 3. (a) Configuration of the box calorimeter used for measurements of absorption. (b) Absorption and transmission past a cylindrical, 10-μm-diam carbon target at an intensity $\sim 10^{15}$ W/cm^2. (c) Angular dependence of absorption on glass disk targets.

does show a peak at $\theta = 25°$ and is qualitatively similar to that which would be expected for resonance absorption of p-polarized laser light in a steepened profile on a planar target.

THERMAL AND SUPRATHERMAL ELECTRON TEMPERATURE MEASUREMENTS

The thermal (T_c) and suprathermal (T_h) electron temperatures were measured with a seven-channel broadband x-ray spectrometer which uses K-edge filters and p-i-n diode detectors. Measured values for T_h were in the 3—5 keV range and are similar to those measured at the same average intensity ($\sim 6\times 10^{14}$ W/cm^2) and the same laser pulse duration for circular laser spots of the same cross-sectional area.[8] The thermal temperature measured for line-focus conditions (200—300 eV) was about 100 eV lower than the thermal temperatures for circular-focus conditions.[8]

ELECTRON DENSITY PROFILE MEASUREMENTS

The electron-density profile for $1.4n_c \gtrsim n_e \gtrsim 0.05n_c$ (where n_e is the electron density and n_c is the critical density) was measured at various times relative to the peak of the laser pulse using an ultraviolet ($4\omega_0$) double-pulse holographic interferometer which has been described elsewhere.[9] The time accuracy of the probe relative to the main pulse was measured experimentally to be ± 5 ps; however, hydrocode simulations are only consistent with the experiment if the probe pulse actually arrived ~ 20 ps later than what was thought experimentally. For consistency of presentation it will be assumed that this was in fact the case; thus "$t = 20$ ps" refers to a time 20 ps after the peak of the pulse in the simulations, and to a probe which was believed (on the basis of experimental timings) to arrive at the peak of the pulse. However, it should be recognized that the simulation results may be "mistimed" by ~ 20 ps due to inadequate modeling of the early-time hydrodynamics. The relative timing of the probe, i.e., the accuracy with which probe delays were measured with respect to one another, was also ± 5 ps and is not in question.

No fringes were visible at or before $t = 0$ ps, indicating that negligible preconditioning of the target surface by low-level laser emission occurred prior to the incidence of the laser pulse. Interferograms are shown for times from 20 to 440 ps in Fig. 4 and illustrate a number of features of the expansion. At early times the expansion is approximately uniform over the full length of the focal line, reflecting the good uniformity of the intensity distribution. At the earliest times ($t = 20$ ps) the fringes are relatively asymmetrical with the expansion occurring preferentially from the irradiated side. By 90 ps, however, plasma extends 20—30 μm behind the target and at late times ($t \sim 440$ ps) the fringe structure is quite symmetrical. This behavior can be interpreted either as due to rapid transport of the absorbed energy by fast electrons to the rear surface, or as a result of flow of the thermal plasma from the irradiated surface around the sides of the target. Attempts to distinguish between these two effects by taking interferograms along the axis of the fibers were unsuccessful, due to refraction of the probe radiation by the long plasma.

At late times ($t \sim 240$—440 ps) some large-scale modulation of the fringes in the low-density region has developed, indicating that the isodensity contours have become rippled. At $t = 20$—90 ps the separation of the π and 3π fringes is large in comparison with that of the other fringes. Corresponding density profiles are shown in Fig. 5(a), where this feature of the fringe behavior translates into a plateau in the density profile close to $n_c/4$. The density in the plateau reduces somewhat between $t = +20$ ps and $t = +90$ ps, and at later times [$t > 140$ ps, Fig. 5(b)] the plateau is not observed at all.

A similar plateau near $n_c/4$ has been reported in interferometric studies of CO_2 laser-produced plasmas,[10] and was attributed to profile modification by the ponderomotive force associated with plasma waves excited at $n_c/4$ by either the two-plasmon decay instability or the absolute Raman instability. To investigate this possibility a search was made for harmonic light associated with these instabilities. Coherent visible emission in the region of 709 nm ($3\omega_0/2$ harmonic most probably due to the two-plasmon decay instability) in the backscattered direction within the aperture of the focusing lens was not observed above the

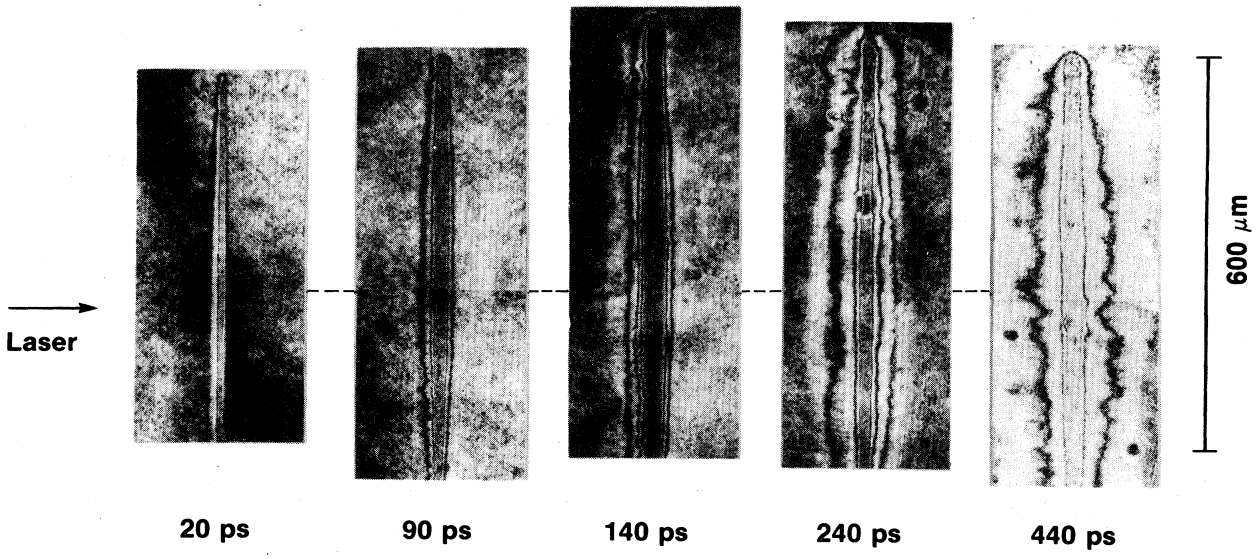

FIG. 4. Picosecond holographic interferograms of plasmas created from carbon cylinders, at various times relative to the peak of the laser pulse.

background continuum for this plasma. Nor was any emission observed in the range 1.2—3.0 μm within 30° and 90° relative to the beam axis, which could have been attributable to stimulated Raman scattering below $n_c/4$.

Computer simulations of the expansion of the electron-density profile, to be described in detail below, are shown as dashed lines in Fig. 5(a). The experiment and simulation are seen to be in reasonably close agreement. The comparison is very sensitive to the relative timing between the two: Thus, if a calculated profile taken just 6 ps later were used to compare with the experimental profile labeled "$t=20$ ps," exact agreement would be obtained for the region between half and quarter critical. There are, however, two notable differences. First, the interferometry clearly cannot provide information on the steep rise of the density profile above critical towards solid density at ~ 5 μm from the target axis. Second, and of greater interest, the simulation does not show the formation of a density plateau in the region of $n_c/4$. These simulations do not include models for energy deposition due to parametric processes; just inverse bremsstrahlung, and resonance absorption at the critical surface, are modeled. Thus, if this plateau is a result of the hydrodynamic flow of the plasma, there must be some physical mechanism operative in the experiment which is not satisfactorily modeled in the hydrodynamic simulations. As

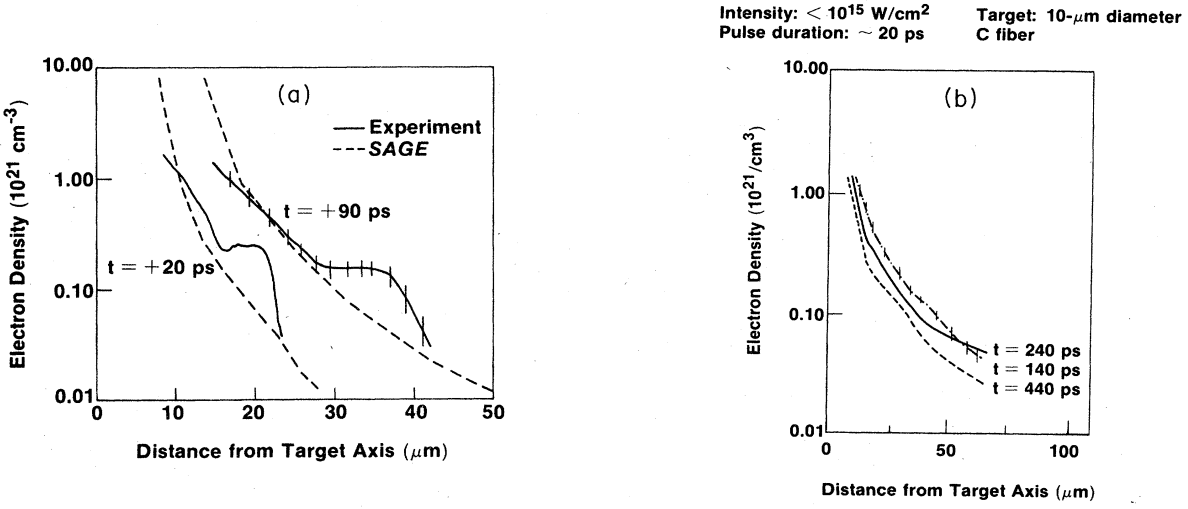

FIG. 5. Axial electron-density profiles of plasmas created from carbon fibers at different times after the laster pulse: (a) at early times, 20 and 90 ps with respect to the peak of the laser pulse, and (b) at late times, 140, 240, and 440 ps. The dashed curves in (a) are SAGE predictions, taken from Figs. 6(b) and 6(c) along the axis $y=0$, for a simulation with a 15% "dump" into resonance absorption and a flux limiter of 0.03.

discussed above, no evidence was found for the existence of the two-plasmon decay or Raman instabilities, which could otherwise provide plausible explanations for the plateau. Assuming that these mechanisms are not operative, another possible cause could be the creation of macroscopic or microscopic magnetic fields which might influence the two-dimensional hydrodynamic expansion.

THEORETICAL SIMULATIONS OF PLASMA EXPANSION

Simulations of these experiments have been carried out in two dimensions with the Eulerian hydrodynamics code SAGE.[7] Resonance absorption is modeled in the code by an *ad hoc* prescription in which a fraction (typically 15%) of the energy reaching the critical surface is deposited into a suprathermal component of hot electrons. These electrons are assumed to have a Maxwellian distribution described by a hot temperature T_h, which is obtained from the local intensity according to the model of Estabrook and Kruer.[11] Inverse-bremsstrahlung absorption, treated in these calculations in conjunction with a ray-tracing model for beam propagation, accounted for no more than a few percent of the incident energy in most of the calculations. The total absorption fraction calculated was therefore dominated by the 15% deposition into resonance absorption. The thermal electron temperature in the coronal region T_c is dependent on the energy transport between the critical and ablation regions. Thermal transport is modeled in SAGE, as in other laser fusion codes, by limiting the heat flux to $f(n_e kT_c)(kT_c/m_e)^{1/2}$ where k is Boltzmann's constant and m_e is the electron mass. Generally flux-limit parameters f of $\lesssim 0.1$ are found necessary to model planar and spherical experiments at $\gtrsim 10^{14}$ W/cm^2; in the present calculations we have used $f=0.03$ (unless otherwise indicated). An ideal-gas equation of state was also used for the carbon targets.

Two-dimensional SAGE calculations of these experiments were run in Cartesian geometry assuming a rectangular-profiled (i.e., spatially uniform) pulse in a collimated beam of 20-μm diameter (overfilling the target by a factor of 2), with a Gaussian pulse shape of duration 20 ps (FWHM) and peak intensity 10^{15} W/cm^2. The target was assumed to be a solid carbon rod of diameter 10 μm. The shape and extent of the electron-density distribution were examined at several times in the expansion of the plasma corona. Figure 6 shows the predicted density profiles and ray trajectories at three times relative to the peak of the laser pulse. At the peak of the pulse ($t=0$) only a slight amount of plasma expansion has occurred, and substantial transmission of light is observed at the edge of the beam. By $t=+20$ ps, the plasma has expanded sufficiently to cut off this transmission. Integrated over the whole simulation, 30% of the incident light is predicted to emerge within the collection cone ($\pm 27°$) of an $f/1$ lens. In the discussion of Fig. 3(b) above, rather more light was transmitted experimentally, but this may be on account of the energy contained further out in the wings of the beam spatial profile. Figure 6(b) supports the possibility, discussed earlier, of a small error in the absolute

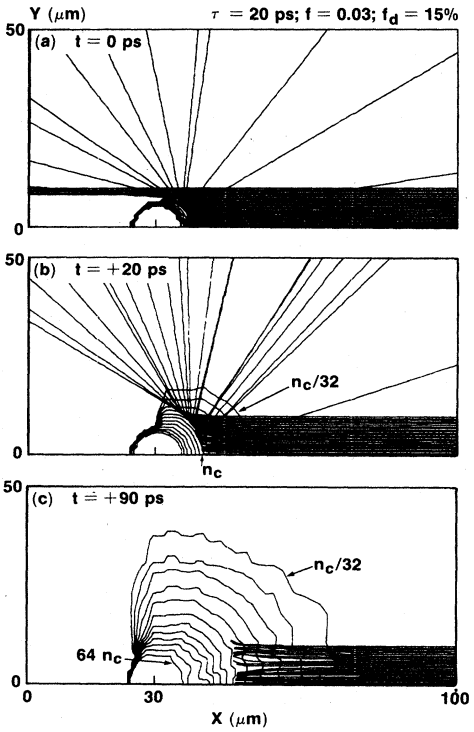

FIG. 6. Two-dimensional SAGE calculation of electron-density contours of plasma expanding from a 10-μm-diam cylindrical target. The simulation is performed in Cartesian geometry in a plane perpendicular to the axis of the cylinder. The laser is incident from the right, and has a diameter twice the target diameter. Rays are not plotted after they have deposited 90% of their energy (as occurs in the colder plasma at +90 ps). Contours are shown from $n_c/32$ to $64n_c$ with the contour interval a factor of 2.

experimental timing of ~ 20 ps since, if the plasma shown in Fig. 6(b) were already formed at the peak of the pulse, it would be hard to account for the $\gtrsim 50\%$ transmission found in Fig. 3(b). Later in time [Fig. 6(c)] the plasma is larger and colder, and the rays undergo 90% absorption before reaching their turning points. The intensity at this time, however, is negligible. The wiggles in the contours of this figure are believed to be numerical noise. The total absorption for this run was 12%, of which 3% was due to inverse bremsstrahlung. While this was lower than observed, the total energy deposited in the plasma was probably comparable, since the estimated experimental intensity was about half the intensity of 10^{15} W/cm^2 used in the simulation. Too much weight should not be attached to the calculated absorption, though, as fast-ion energy losses are not modeled.

The lateral spreading evidenced in Fig. 6 is, perhaps surprisingly, more dependent on the thermal flux limiter f than on parameters related to the multigroup flux-limited diffusion model used for the suprathermal electrons. For example, a run omitting suprathermal electrons but using $f=0.65$ showed a somewhat greater spreading rate than occurs in Fig. 6, with plasma having almost reached the

TABLE I. Parameters of runs A–F.

Run	Dimension	Nominal intensity (W/cm^2)	Suprathermal electrons?	Flux limiter f	Equation of state
A	2D	10^{15}	Yes	0.03	Ideal gas
B	1D	10^{15}	Yes	0.03	Ideal gas
C	1D	5×10^{14}	Yes	0.03	Ideal gas
D	1D	10^{15}	No	0.03	Ideal gas
E	1D	10^{15}	No	0.65	Ideal gas
F	1D	10^{15}	No	0.65	SESAME

rear axis by +90 ps. In any case it is probable that Fig. 6 represents an underestimate of the rate of lateral energy flow since the important effect of magnetic-field-enhanced lateral transport[12] is not modeled in SAGE.

Experimental data for the time history of the trajectories of the n_c, $n_c/4$, and $n_c/10$ points along the laser axis are shown in Fig. 7 for a 10-μm-diam cylindrical carbon target. The data points are derived from profiles such as illustrated in Fig. 5. The dashed curves are SAGE predictions for the n_c and $n_c/10$ contours. During the laser pulse, and up to 100 ps after the peak of the pulse, theory and experiment are in close agreement. Both are also consistent with the critical-surface velocity of $(1.5\pm0.5)\times10^7$ cm/sec inferred from the Doppler shift of the second-harmonic spectrum (see below). At times greater than 100 ps, however, theory and experiment diverge markedly.

Several runs (see Table I) were performed to investigate this discrepancy, mostly in one-dimensional cylindrical geometry on the grounds that lateral transport should be sufficient to make the late-time plasma expansion approximately one-dimensional. In this geometry the rays are assumed to be incident normal to the target, with an intensity reduced (from the nominal values shown in Table I) by a factor of π since the irradiated area per unit length of fiber is increased by a factor of π. Thus the actual peak intensity of run B is 3×10^{14} W/cm^2. Predictions of the trajectories of the tenth-critical and critical surfaces, for each of the runs A–F listed in Table I, are shown in Figs. 8 and 9, respectively. In each figure the experimental data (taken from Fig. 7) are also shown for comparison.

Run A is the two-dimensional simulation used for Figs. 5–7. Run B, the one-dimensional version of run A, exhibits very similar behavior. The initial expansion of the two trajectories is somewhat slower, because the actual intensity is lower, but the late-time behavior is not greatly different. Run C, at half the intensity of run B, shows reduced excursions for both $n_c/10$ and n_c, but not enough to explain the late-time behavior. This indicates that uncertainties in the experimental intensity, which are at the most a factor of 2, are not the cause of the discrepancy.

Some insight into the role of suprathermal electrons is provided by run D, which was as run B except that suprathermal electrons were excluded. The predicted excursions at late time of both tenth-critical and critical surfaces are much closer to experiment, whereas the excursions in the first $\sim$100 ps after the peak of the pulse are far too small. In run B, energy deposition from the

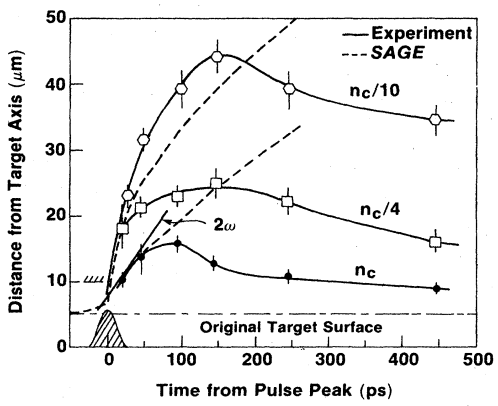

FIG. 7. Trajectories of the n_c, $n_c/4$, and $n_c/10$ points along the laser axis, from a solid carbon cylinder target. Solid curves, experiment; dashed curves, SAGE predictions for the n_c and $n_c/10$ trajectories. The line labeled "2ω" indicates the critical-surface velocity $[(1.5\pm0.5)\times10^7$ cm/sec] obtained from the second-harmonic spectrum. Before $t=0$, no plasma was seen beyond a distance 10 μm from the target axis.

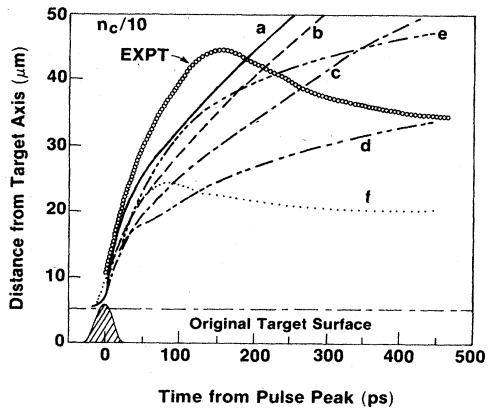

FIG. 8. Calculated $n_c/10$ trajectories for various runs A–F (see Table I). Run A is the two-dimensional simulation of Figs. 5–7.

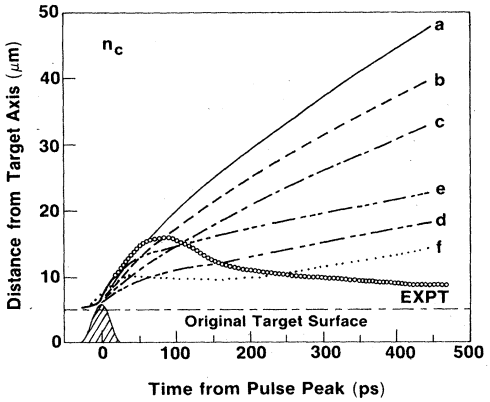

FIG. 9. Calculated n_c trajectories for runs A—F.

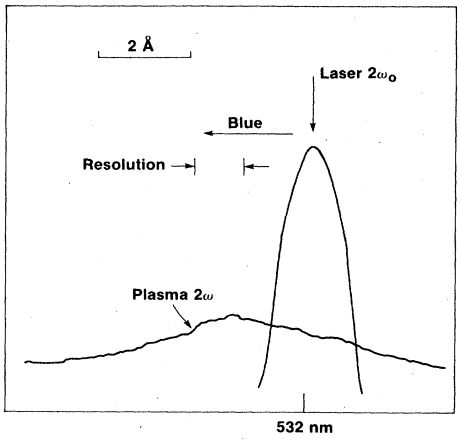

FIG. 10. Spectral shift and broadening of the backreflected second-harmonic emission, from which an estimate of the expansion velocity of the n_c surface during irradiation is obtained.

suprathermal electrons into the coronal plasma leads to large excursions at $t \approx +100$ ps, and deposition into densities around solid (causing low-temperature preheat) leads to strong plasma expansion at late times. It may be that the calculations overestimate this preheat, as would be the case in the presence of any mechanism (e.g., magnetic fields[12]) tending to confine suprathermal electrons within the corona. Another effect not modeled is the electrostatic acceleration due to the electric field generated by the suprathermals, which may be alternatively thought of as an additional pressure due to suprathermals. In run A, in the corona and at the peak of the pulse, the number density and temperature of suprathermal electrons are around 4×10^{19} cm^{-3} and 10 keV, respectively, implying a significant expansion force in the underdense corona. It is possible that this force, operative primarily during the laser pulse, gives rise to the density perturbation seen in Fig. 5(a) which is subsequently convected down the density gradient into the corona.

The effect of the flux limiter is seen by comparing runs D ($f=0.03$) and E ($f=0.65$). In run E, larger excursions are observed and, although the late-time trajectories diverge from experiment, the early behavior is quite close to the experiment. It should not, however, be inferred that the heat is "uninhibited," since suprathermal electrons were excluded from this run: The effect of the higher value of f is to provide better heat transport to densities above critical, mimicking deposition by suprathermals.

The most obvious source of disagreement between simulation and experiment at late times is the treatment of the plasma as an ideal, fully ionized gas in runs A—E: after the laser pulse is over the corona should cool and the carbon recombine. In run F, the (local-thermodynamic-equilibrium) SESAME (Ref. 13) equation of state is used; the parameters of this run are otherwise the same as those of run E, except that CH was used in place of carbon for which SESAME tables are unavailable. The critical and tenth-critical trajectories of these two runs are very close at early times (when the plasma is predicted to be fully ionized), but diverge at later times due to recombination. The trajectories of run F do not come close to reproducing the peak experimental excursions. It therefore appears that the inclusion of time-dependent (nonequilibrium) recombination would be necessary to model the slow plasma recombination and the full time history of the electron-density contours.

PLASMA PROFILE VELOCITY FROM SECOND-HARMONIC SPECTRUM

Independent information on the critical surface velocity during the pulse was obtained from spectral measurements of the second harmonic emitted back into the aperture of the focusing lens. The spectrum was analyzed using a McPherson 2051 spectrometer. The resolution in these measurements was limited to ~1 Å on account of the poor imaging properties of the astigmatic lens, since a relatively wide slit was necessary in order to obtain sufficient light input. A typical spectrum (Fig. 10) shows that the second-harmonic line is considerably broader than the reference line produced by frequency doubling part of the main laser pulse, and has its peak blue shifted by (2 ± 1) Å. This can be interpreted as the influence of the Doppler effect on $2\omega_0$ light generated by resonance absorption at an expanding critical density surface. The average expansion velocity can then be calculated to be $\sim1.5\times10^7$ cm/sec, which agrees well with both the data obtained by interferometry and the code predictions.

INTERFEROMETRY AND POLARIMETRY OF UNDERDENSE PLASMA EXPANSION

Additional information on the plasma expansion was obtained using conventional interferometry with simultaneous polarimetry (Faraday-rotation measurements). In this case the probe wavelength of 630 nm was obtained by Raman shifting the laser second harmonic in ethanol. The optical arrangement for simultaneously obtaining interferograms and polarograms consisted of a modified Nomarski interferometer using a 2° calcite Wollaston prism in which the reference beam was removed, by a

beam stop, from one of the complementary interferograms in order to generate a polarogram. The pair of images thus formed were approximately in the same plane, simply shifted laterally from one another but having otherwise passed through an identical spatial system.[14] The optics could be focused to an accuracy of about 10 μm using a HeNe laser to backlight a carbon fiber target. This optical arrangement has the virtue of considerable simplicity and presents the data in a form in which it is easy to visually compare the behavior of the Faraday rotation signal and the plasma expansion (as indicated in the interferogram), allowing the magnetic-field and plasma structures to be related qualitatively. The data were recorded on Kodak Tri-X negative film whose sensitivity was pushed when necessary to 1600 ASA.

This interferometer measured densities in the range $0.01 n_c < n_e < 0.2 n_c$ and proved particularly sensitive to the presence of nonuniformities in the expanding plasma. For all target types, regular striations normal to the target surface were visible in both the interferograms and the polarograms. These striations extended to the edge of the corona from the highest probed densities and were also visible in the plasma expanding on the rear side of the 1000-Å-thick carbon foils. A typical time sequence of polarograms and interferograms showing the development of these striations in a plasma generated on disk targets is shown in Fig. 11. Such structures have been observed in the expanding coronas of plasmas produced by nanosecond laser pulses on both microballoons and planar targets.[15] It has been suggested[15] that the characteristic dark/light pattern observed near one such filament indicates the presence of large megagauss self-generated magnetic fields surrounding the filaments. This possibility was examined in our case by further modifying the Nomarski system so that the reference beams were removed from both images. In this case, a pair of complementary polarograms were obtained in which Faraday rotation would produce a reversal of the dark/light pattern between the two images. As is evident from Fig. 12, no such behavior was observed, and scans of equivalent parts of the images using a microdensitometer were indistinguishable.

The striations cannot thus be associated with strong magnetic fields, although fields below ~ 100 kG (the approximate sensitivity of the detection system) cannot be ruled out. It would, therefore, appear that the striations are due to density modulations or jets in the plasma which cause refraction (and possibly depolarization) of the probe beam. The interferograms of Fig. 11 show fringe modulation with the same spatial scale as the jets, in support of this inference. However, there appears to be little correlation between the structure of the jets in the polarogram and either inward or outward deflection of the fringes. This may not be surprising since refractive effects would be more sensitive to density gradients normal to the jet axis, whilst the fringe shifts are proportional to the integrated density along the ray path and these two quantities are only rather indirectly related.

As in the previous work,[15] however, these observations do indicate that the corona is unstable to some kind of hy-

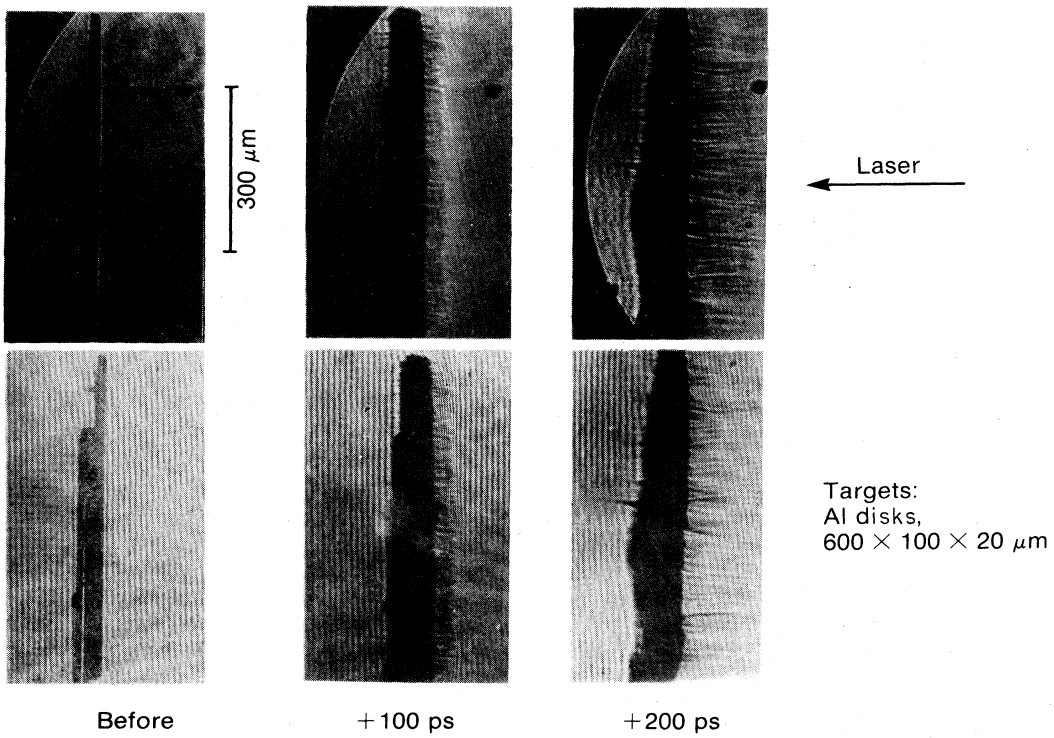

FIG. 11. Polarograms and interferograms of the expansion of plasmas from disk targets, showing the evolution of filamentary structure in the corona.

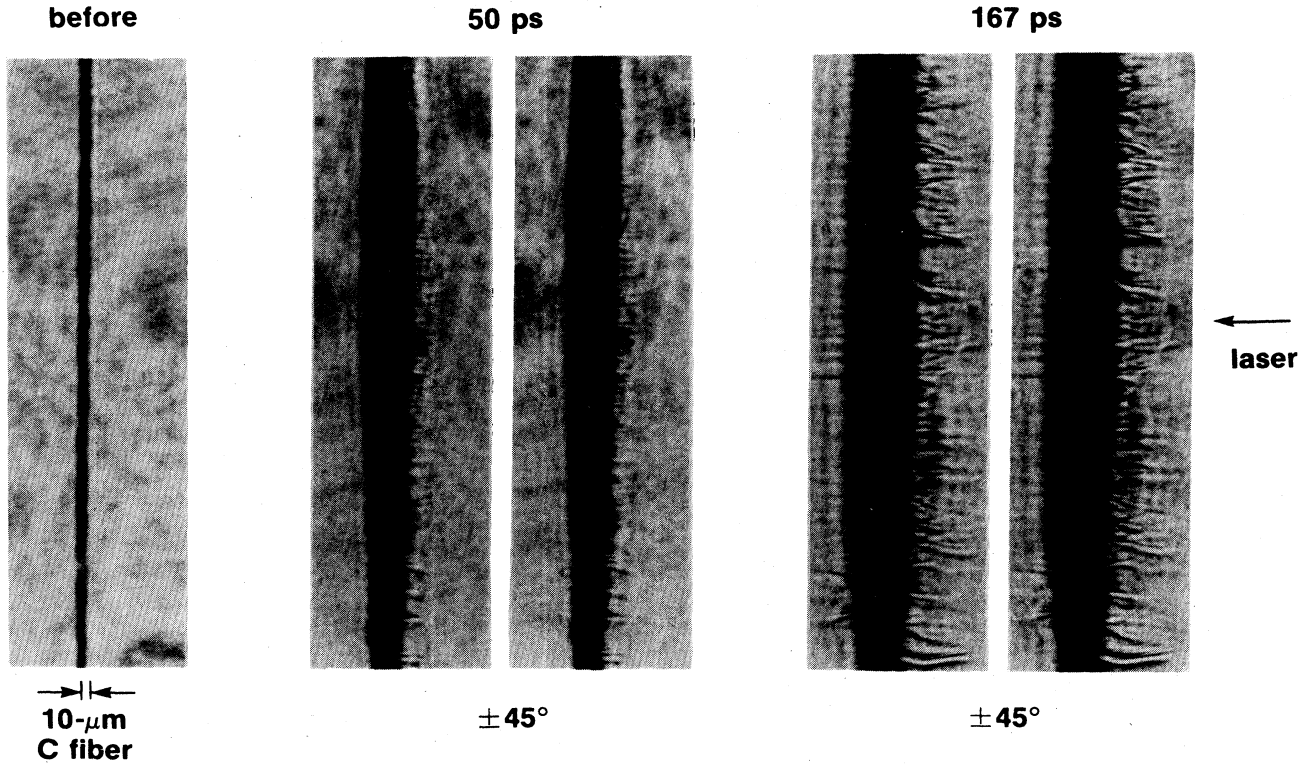

FIG. 12. Complementary polarograms of the plasma produced from a thin foil target.

drodynamic instability which is largely unaffected by changes in the target or its surface conditions. (Larger-diameter glass fibers with surfaces which were initially smooth in comparison with the carbon fibers gave very similar striations.) Since it is the underdense coronal region in which the inversion typically occurs in recombination laser systems, significant density modulations could markedly affect the expected gain by both modulating the population inversion produced along the line and possibly refracting x rays out of the plasma before significant amplification can occur.[16]

SUMMARY

The measurements reported here represent the first study devoted to the characterization of a cylindrical plasma created by picosecond laser pulses. Laser-produced plasmas of this general form are becoming of importance because of their potential as x-ray laser media. For most x-ray laser schemes, a precise knowledge of the density and temperature profiles in the underdense region of the plasma is a necessary prerequisite to an understanding of the ionization state distribution and the level population density. Moreover, the coherent amplification of x rays in laser-generated plasma will only be efficient in a spatially homogeneous medium.

The present study has focused on the characterization of the electron-density distribution for thin foils and small-diameter solid cylindrical targets. Irradiated with intense ($> 10^{14}$ W/cm^2), short-pulse (20 ps) 1.06-μm laser light, these plasmas are produced with copious fluences of suprathermal electrons generated by resonance absorption. These electrons tend to smooth out nonuniformities in the plasma created by illumination nonuniformities and hydrodynamic instabilities. Plasmas produced by short-wavelength lasers, in which absorption by inverse bremsstrahlung occurs at high densities and closer to the ablation surface, are likely to be less forgiving of spatial structure in the laser-beam profile.

The initial expansion of the plasmas described in this study is fairly well modeled by flux-limited SAGE calculations. However, a distinct plateau in the profile appears at $\sim n_c/4$, which is not accounted for in the simulations; nor is there any evidence, to the level of detectivity, for profile steeping produced by stimulated Raman scattering or the two-plasmon decay instability. The plasma dynamics are probably influenced by suprathermal electrons, which may be responsible for this density plateau. At later times in the expansion the code models the plasma flow less well. This most likely arises as a consequence of the detailed nonequilibrium recombination and ionization processes underway in the outer corona. It is clear that in order to support x-ray laser studies concentrating on collisional or recombination processes, two-dimensional hydrodynamic simulations of recombining plasmas will have to take account of these processes.

The detailed interferometry and polarimetry of the outer plasma reveal unexpected small-scale structures which appear to grow with the plasma expansion. Although it is not clear what causes this phenomenon, there are a variety of possible explanations: filamentation induced by hot electrons,[17] microscopic magnetic fields

which create stable expanding spicules,[15] thermal instabilities,[18] or microscopic contaminants, perhaps of different Z, on the surface of the target.[19] Irrespective of the cause, it is clear that such microscopic structures will have a significant effect on the characteristics for x-ray gain in the underdense region.

ACKNOWLEDGMENTS

The contributions to this work performed by M. C. Richardson and R. S. Craxton were supported by the U.S. Department of Energy Office of Inertial Fusion under agreement No. DE-FC08-85DP40200 and by the Laser Fusion Feasibility Project at the Laboratory for Laser Energetics, which has the following sponsors: Empire State Electric Energy Research Corporation, General Electric Company, New York State Energy Research and Development Authority, Northeast Utilities Service Company, Ontario Hydro (Canada), Southern California Edison Company, The Standard Oil Company, and the University of Rochester. The participation of one of us (M.C.R.) in the majority of these experiments was performed under support by the Australian National University Visiting Fellow Program.

[1]For reviews of short-wavelength laser research, see R. W. Waynant and R. C. Elton, Proc. IEEE **64**, 1058 (1976); R. C. Elton, in *Handbook of Laser Science and Technology,* edited by M. J. Weber (CRC Press, Cleveland, 1980); F. V. Bunkin, V. I. Derzhiev, and S. I. Yakovlenko, Kvant. Elektron. **8**, 1621 (1981) [Sov. J. Quantum Electron. **11**, 981 (1981)].

[2]G. J. Tallents, J. Phys. B **11**, L157 (1978); U. Furukane, T. Yokota, K. Kawasaki, and T. Oda, J. Quant. Spectros. Radiat. Transfer **29**, 75 (1983).

[3]Y. Conturie, B. Yaakobi, J. Delettrez, and J. M. Forsyth, *Laser Techniques for Extreme Ultraviolet Spectroscopy,* Subseries on Optical Science and Engineering Number 2, Proceedings of the Topical Meeting on Laser Techniques for Extreme Ultraviolet Spectroscopy, AIP Conf. Proc. No. 90, edited by T. J. McIlraith and R. R. Freeman (AIP, New York, 1982), p. 312.

[4]L. I. Gudzenko and L. A. Shelepin, Dokl. Akad. Nauk. SSSR **160**, 1296 (1965) [Sov. Phys. Dokl. **10**, 147 (1965)]; G. J. Pert, J. Phys. B **9**, 1 (1976).

[5]D. Jacoby, G. J. Pert, L. D. Shorrock, and G. J. Tallents, J. Phys. B **15**, 3557 (1982).

[6]D. L. Matthews *et al.*, Phys. Rev. Lett. **54**, 110 (1985); M. D. Rosen *et al.*, *ibid.* **54**, 106 (1985).

[7]R. S. Craxton and R. L. McCrory, J. Appl. Phys. **56**, 108 (1984); see also R. S. Craxton and R. L. McCrory, Laboratory for Laser Energetics Report No. LLE-99 (1980) and No. LLE-108 (1980) (unpublished).

[8]M. D. J. Burgess, R. Dragila, B. Luther-Davies, K. A. Nugent, and G. J. Tallents, *Laser Interaction and Related Plasma Phenomena,* edited by H. Hora and G. H. Miley (Plenum, New York, 1984), Vol. 6, p. 461.

[9]M. D. J. Burgess, G. B. Gillman, and B. Luther-Davies, J. Appl. Phys. **54**(4), 1787 (1983).

[10]H. A. Baldis, J. G. Samson, and P. B. Corkum, Phys. Rev. Lett. **41**, 1719 (1978).

[11]K. Estabrook and W. L. Kruer, Phys. Rev. Lett. **40**, 42 (1978).

[12]D. W. Forslund and J. U. Brackbill, Phys. Rev. Lett. **48**, 1614 (1982); M. A. Yates, D. B. van Hulsteyn, H. Rutkowski, G. Kyrala, and J. U. Brackbill, *ibid.* **49**, 1702 (1982).

[13]B. I. Bennett, J. D. Johnson, G. I. Kerley, and G. T. Rood, Los Alamos National Laboratory Report LA-7130, 1978 (unpublished).

[14]J. A. Stamper, E. A. McLean, S. P. Obenschain, and B. H. Ripin, NATO Advanced Study Institute Lectures on Fast Electrical and Optical Diagnostic Principles and Techniques, Castelvecchio Pascoli (Lucca), Italy, 1983 (unpublished).

[15]O. Willi and P. T. Rumsby, Opt. Commun. **37**(1), 45 (1981).

[16]P. L. Hagelstein, Plasma Phys. **25**, 1345 (1983).

[17]K. Estabrook, Phys. Rev. Lett. **41**, 1808 (1978); O. Willi, P. T. Rumsby, C. Hooker, A. Raven, and Z. Q. Lin, Opt. Commun. **41**, 110 (1981).

[18]M. G. Haines, Phys. Rev. Lett. **47**, 917 (1981).

[19]M. J. Herbst, R. R. Whitlock, and F. C. Young, Phys. Rev. Lett. **47**, 1568 (1981).

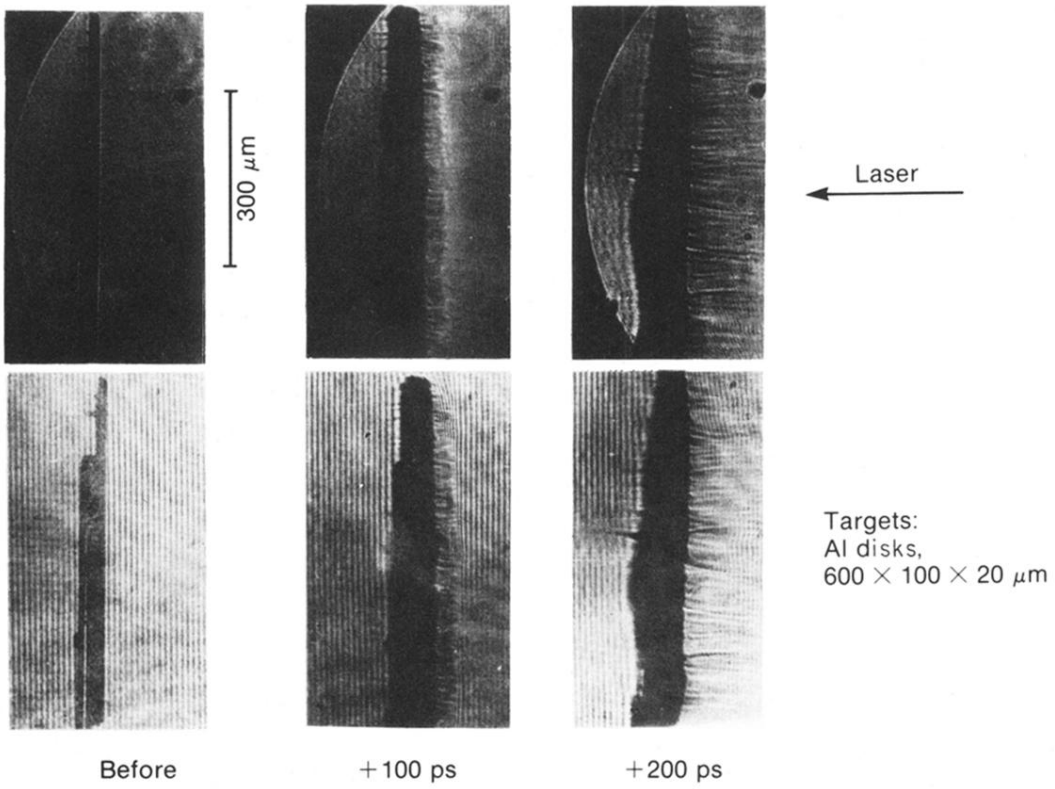

FIG. 11. Polarograms and interferograms of the expansion of plasmas from disk targets, showing the evolution of filamentary structure in the corona.

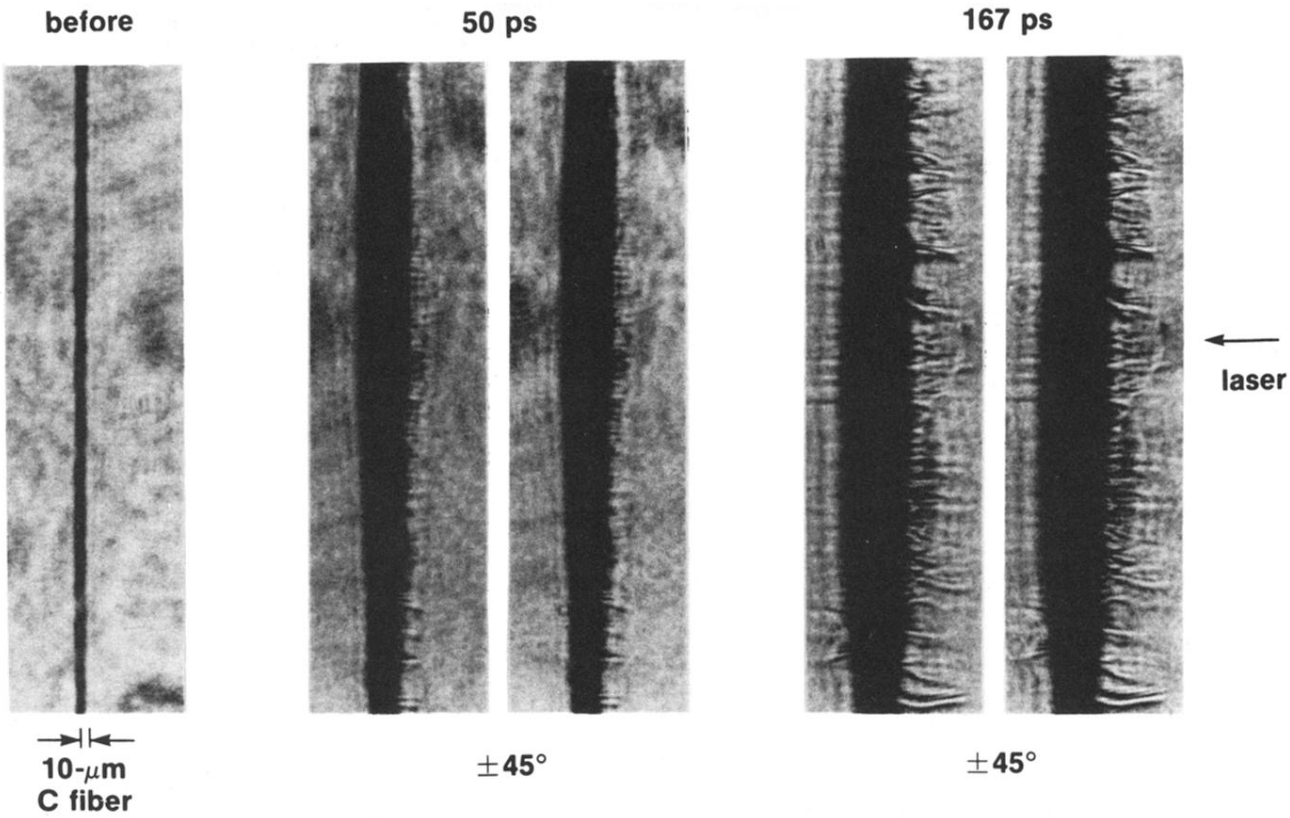

FIG. 12. Complementary polarograms of the plasma produced from a thin foil target.

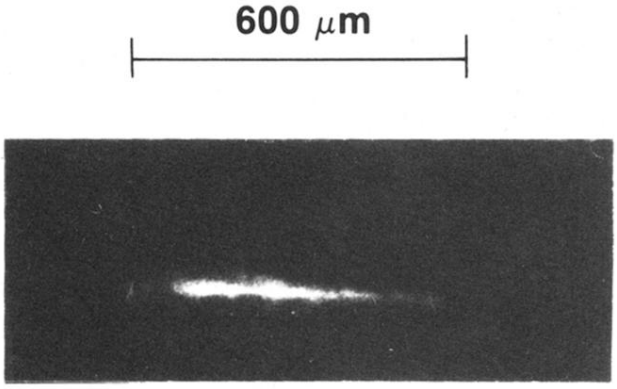

FIG. 2. X-ray micrograph of a line-focused plasma produced from a solid Al target, obtained with a Kirkpatrick-Baez microscope sensitive to x rays in the ~1-keV range.

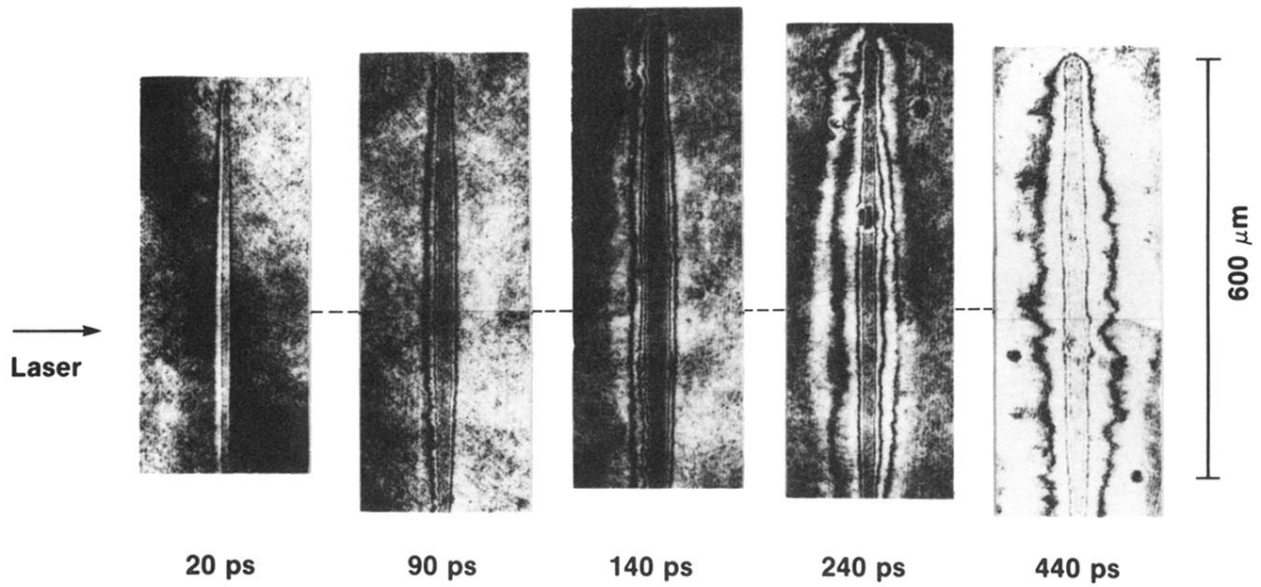

FIG. 4. Picosecond holographic interferograms of plasmas created from carbon cylinders, at various times relative to the peak of the laser pulse.